Mesopotamian Journal of Computer Science

Volume 6 | Issue 1 Article 1

4-3-2026

A Hybrid XFEM-ML Framework for High-Fidelity, Rapid Fracture Prediction in Cortical Bone: From Microstructure to Clinical Translation

Noor T. Al-Sharify
Medical Instrumentation Engineering Department, Al-Esraa University, Baghdad, Iraq AND Department of Electrical & Electronic Engineering, College of Engineering, Universiti Tenaga Nasional, Kajang 43000, Malaysia, n2021@esraa.edu.iq

Ammar Fadhil Hussein AL-Maliki
Mechanical Engineering Department College of Engineering, Mustansiriyah University, Baghdad 10052, Iraq, ammarfadhil@uomustansiriyah.edu.iq

Ahmed Ali Farhan Ogaili
Mechanical Engineering Department College of Engineering, Mustansiriyah University, Baghdad 10052, Iraq, ahmed_ogaili@uomustansiriyah.edu.iq

See next page for additional authors

A Hybrid XFEM-ML Framework for High-Fidelity, Rapid Fracture Prediction in Cortical Bone: From Microstructure to Clinical Translation

Authors

Noor T. Al-Sharify, Ammar Fadhil Hussein AL-Maliki, Ahmed Ali Farhan Ogaili, Abdul-Rasool Kareem Jweri, Alaa Abdulhady Jaber, and Luttfi A. Al-Haddad

RESEARCH ARTICLE

A Hybrid XFEM-ML Framework for High-Fidelity, Rapid Fracture Prediction in Cortical Bone: From Microstructure to Clinical Translation

Noor T. Al-Sharify [a,b], Ammar Fadhil Hussein AL-Maliki [c], Ahmed Ali Farhan Ogaili [c,*], Abdul-Rasool Kareem Jweri [d], Alaa Abdulhady Jaber [e], Luttfi A. Al-Haddad [e]

[a] Medical Instrumentation Engineering Department, Al-Esraa University, Baghdad, Iraq
[b] Department of Electrical & Electronic Engineering, College of Engineering, Universiti Tenaga Nasional, Kajang 43000, Malaysia
[c] Mechanical Engineering Department College of Engineering, Mustansiriyah University, Baghdad 10052, Iraq
[d] College of Agricultural Engineering Sciences, University of Baghdad, Baghdad, Iraq
[e] College of Mechanical Engineering, University of Technology-Iraq, Baghdad 10066, Iraq

ABSTRACT

This paper proposes a hybrid computational model, which combines the eXtended Finite Element Method (XFEM) with machine learning (ML) to forecast the fracture behavior of cortical bone while maintaining microstructural fidelity. It has created a parametric dataset of about 450 three-dimensional XFEM models of single-edge notched bend (SENB) specimens, including important μ-structure features (e.g., osteon orientation, cement line properties, interfacial connectivity, etc.). Based on these simulations, 47 quantitative descriptors were obtained, and these were used to model supervised ML models, namely, Random Forest and Artificial Neural Networks, to estimate fracture load. The Random Forest model demonstrated exceptional predictive performance ($R^2 = 0.952$, MAE = 6.1 N, MAPE = 1.9%, Pearson r = 0.980), significantly outperforming the ANN model ($R^2 = 0.831$, MAE = 11.8 N, MAPE = 3.7%), The Random Forest model demonstrated strong predictive performance ($R^2 = 0.95$, MAE = 6.1 N, MAPE = 1.9%), while reducing computational time by nearly 300-fold and memory requirements by over 20-fold compared to full XFEM analyses. For fracture resistance, feature importance analysis indicated the most salient features were osteon orientation, cement line strength, and pore topology. The methodology was also robust, as further led to by sensitivity analyses and uncertainty quantification. The hybrid method provides microstructure-based predictions of fracture that are very automated and precise and result in a significant decrease in computational cost, hence allowing a scalable route to clinical translation to characterize bone integrity.

Keywords: Cortical bone, Fracture Load prediction, Extended finite element method, Machine learning, Computational efficiency, Biomedical

1. Introduction and literature review

Fracture of the cortical bones that are predictable has become one of the biggest challenges to address and critical clinical impacts to the ever-growing aging population of the world. Recent epidemiological studies have shown that more than 8.9000, 000 individuals annually die as a result of osteoporotic fractures, and this number is spread across the world, causing a critical health-care resource burden, and low quality of life [1]. Conventional clinical evaluation instruments, such as the Fracture Risk Assessment Tool

Received 3 October 2025; revised 5 December 2025; accepted 25 January 2026.
Available online 3 April 2026

* Corresponding author.
E-mail addresses: n2021@esraa.edu.iq (N. T. Al-Sharify), ammarfadhil@uomustansiriyah.edu.iq (A. F. H. AL-Maliki), ahmed_ogaili@uomustansiriyah.edu.iq (A. A. Farhan Ogaili), abdulrasool.k@coagri.uobaghdad.edu.iq (A-R. K. Jweri), Alaa.a.jaber@uotechnology.edu.iq (A. A. Jaber), Luttfi.a.alhaddad@uotechnology.edu.iq (L. A. Al-Haddad).

https://doi.org/xx.xxxxx/2958-6631.1070

(FRAX), mainly depend on measurements of bone mineral density and epidemiological risk factors, but they show poor predictive accuracy for specific patients [2, 3]. This kind of natural deficiency is an outcome of inadequate depiction of microstructural heterogeneity that functions with a crucial impact on fracture resistance in cortical bone. The extreme complexity of the hierarchical arrangement of cortical bone, containing nanoscale collagen -mineral complex, microscale osteons and macroscale overall bone structure, poses enormous difficulties to the state of art mechanical modelling [4]. Osteon orientation distributions, cement line distributions, and porosity distributions have the ability to change fracture resistance by factors greater than two-fold, although these key variables are generally not a focus of clinical evaluation procedures [5]. This continued disparity between mechanistic knowledge and clinical application has led to the accumulation of much research on computational approaches that can be used to incorporate microstructural detail, without rendering them impractically challenging. The choice of the method of modelling crack propagation in cortical bone has been the extended finite element method due to its ability to handle discontinuities without remeshing [6]. The anisotropic damage criteria have been developed by the works of Fan et al., who have implemented the orientation-dependent failure models in the XFEM frameworks [7]. In essence, their method of approach was effective in the literal prediction of the strong effects literally of osteon orientation on the direction of crack propagation and fracture toughness, which offers computational confirmation of experimental results on cortical bone anisotropy. In spite of these developments, computational requirements are still prohibitive to actual patient-specific clinical application [8]. The use of machine learning in the field of biomedical engineering has witnessed a phenomenal increase owing to progress in the deep learning architecture as well as more access to medical imaging data. Past research has established that machine learning can detect new risk factors that were not identified before by pattern recognition on a complex and high-dimensional dataset [9]. The study demonstrated machine learning's potential to identify previously unrecognized risk factors through pattern recognition in complex, high-dimensional datasets. Comprehensive systematic reviews by Kuo et al. analyzed over 42 studies applying artificial intelligence to fracture detection across multiple imaging modalities [10]. Building on advances in representation learning, machine learning (ML) has been applied to fracture risk assessment and image-based diagnosis in ways that complement traditional tools. Many of researcher used the powerful of ML with FEA such as, Kong et al. developed a CatBoost model that outperformed FRAX in predicting fragility fractures and surfaced additional predictors beyond bone mineral density, underscoring ML's value for individualized risk stratification [11]. In parallel, deep learning (DL) systems trained on radiographs now achieve high diagnostic accuracy for fracture detection; Aldhyani *et al.* [12] benchmarked VGG16, ResNet152V2, and DenseNet201 on a 10,580-image dataset, reporting strong performance and arguing for automated pipelines in clinical workflows. Models that rely only on data run into hard limits that bar them from use in life critical medical tasks. Modern deep learning supplies the expressive power for those tasks because it extracts layered features from vast data and has reshaped visual pattern recognition and other fields [13]. Yet models that learn from data alone often fail when they must generalize beyond the training set or respect physical laws - this failure drives interest in physics-aware techniques. Physics-Informed Machine Learning (PIML) folds the governing equations, conservation rules or known structure into the learning process, which raises data efficiency and improves behavior outside the training range [14]. As a concrete biomedical example, Naghavi *et al.* [15] embedded cardiovascular dynamics into a physics-informed neural network (PINN) to invert left-ventricular contractility from single-beat data, achieving accurate parameter estimation while preserving physiologic plausibility—illustrating how physics guidance can stabilize learning in safety-critical settings. Complementary to PIML, hybrid finite-element/ML strategies leverage high-fidelity simulations to train fast surrogates. In manufacturing mechanics, George *et al.* [16] linked time histories from finite element models to a neural network that was trained in reverse to yield optimal machining settings - the finite element data trained an ML predictor that performs well in practice.

In applying such a concept to field prediction, Li et al. [17] have proposed a way of re-forming accurate strain fields with a few nodes by a method that is based on ML-based finite element (FE) construction, thereby proving that a substantial efficiency gain can be made without a substantial loss of accuracy. These advances denote how it can be achieved to possess hybrid solutions to the trade-offs between mechanistic precision, and computational efficiency. The validation procedures do not coincide in the different categories of research, and therefore, limit the prospect of comparing and establishing benchmark levels of performance. Uncertainty is also not quantifiable in most of the existing techniques, but it is required in clinical practice where treatment decisions would need to

be made based on the reliability of prediction and risk toleration they require, as presented in the study of [18]. Computational bone mechanics is rapidly progressing in the modern literature that can be attributed to the growth of the imaging technology, computational capabilities, and algorithms. Another promising direction, particularly where physics-based simulation meets machine learning strategies, is a particularly attractive one that cuts across some of the conventional drawbacks of both.

The paper fills the mentioned research gap by developing and validating a novel hybrid AI-XFEM framework, which incorporates a more accurate model of the microstructure with the help of XFEM simulations and effective machine learning predictive models. The framework keeps mechanistic knowledge in a attained performance of computation sufficient to be utilized in the clinic. The traditional XFEM techniques can provide high fidelity predictions of fractures, but at extremely high computational cost (approximately 2 hours per simulation) and can thus not be used in clinical practice. Pure ML methods are data-oriented and do not require physical properties, and they do not embrace microstructural properties, which limits their use in the clinic.

The gaps in the research that are chosen to generate and test a new hybrid AIXFEM model in combining implicit microstructural modeling and XFEM simulation based model with machine-learning based prediction models are filled by the current investigation. The framework does not lose mechanistic knowledge but develops computational abilities, which could be applied in clinical practice.

The key research questions will be the following:

1. Design elaborate XFEM models that are directly based on the significant microarchitectural attributes of cortical bone of osteons, cement lines, and porosity network and compare with literature experimental data.
2. Theoretically simulate parametric data sets of large scale systematic XFEM simulations of the dependence between microstructural parameters and fracture outputs in the regimes of interest to physiological systems.
3. Use machine-learning optimized algorithms (Random Forest and Artificial Neural Networks) to estimate fracture-loads with almost accuracy and perfect quantification of uncertainty.
4. Evaluate the advances in computational effectiveness over conventional XFEM simulation, thereby demonstrating that it is feasible in clinical applications.
5. Regular sensitivity analysis (in order to establish the main microstructural parameters) and identify the main critical limits to be exploited in assessing clinical risk.
6. Comparison of the integrated framework developed with the available experimental results in various microstructural designs.

The substantive findings of the current work are the following: (i) the initial hybrid framework systematically, which can be employed to integrate the extended finite element method (XFEM) simulations with the machine-learning algorithms to predict cortical bone fracture; (ii) the development of highly detailed and three-dimensional microstructural models, which explicitly reflect the heterogeneity of discrete elements; (iii) the systematic identification and prioritization of the microstructural parameters, which have a critical impact on the fracture resistance; (iv) the clarification of greatly enhanced computational efficiency without the reduction of clinically relevant.

2. Materials and methods

2.1. Multi-modal data acquisition protocol

The hybrid AI-XFEM framework consists of four complementary, high-throughput lab-based data acquisition modalities to characterize the effective structural behavior of cortical bone across a wide range of length scales. Clinical computed tomography (CT) provides high spatial resolution of macroscopic geometry and measurements of bone mineral density distribution (0.6 mm) [19] as presented in Table 1. High-resolution micro-computed tomography and synchrotron radiation micro-CT deliver microstructural detail at 2–50 μm resolution, capturing osteon morphology, cement line architecture, and three-dimensional porosity networks essential for physics-based modeling [20]. Natural fractures are excellent for validating computational segmentation algorithms and providing in-situ material composition verification [21], while their mechanical testing supplies ground truth fracture loads and crack propagation data for model calibration.

Finally generated 450 unique XFEM models by systematically varying bone microstructure parameters.

2.2. Material characterization and data integration

2.2.1. Cortical bone material property characterization

Cortical bone exhibits a complex hierarchical organization requiring sophisticated material characterization across multiple constituents [8]. Osteon tissue behaves as if it has the same stiffness in every direction that lies across the long axis of the osteon, but a different stiffness along that axis as

Table 1. Data acquisition protocol specifications.

Modality	Parameters	Output	Integration Method	Spatial Resolution	Clinical Feasibility
Clinical CT	120 kVp, helical scan	Bone geometry, BMD	DICOM processing	0.6 × 0.6 × 0.6 mm^3	Routine clinical use
μCT/SR-μCT	70–90 kVp, 8W power	Microstructural detail	Automated segmentation	2–50 μm isotropic	Research/specialized
Histological	5–7 μm sections, H&E stain	Material validation	Digital microscopy	0.2 μm lateral	Standard laboratory
Mechanical Testing	Three-point bending	Fracture loads	Load-displacement curves	Force resolution ±0.1 N	Post-mortem validation

Table 2. Comprehensive material property database.

Component	Elastic Constants	Strength Parameters	Failure Criteria	Age Dependency	Measurement Method
Osteon Tissue	$E_1 = 18.4 \pm 2.8$ GPa	$\sigma_{ult} = 135 \pm 18$ MPa	Maximum stress	–5.8%/decade	Nanoindentation [7]
	$E_2 = 11.9 \pm 1.7$ GPa	$\sigma c = 205 \pm 25$ MPa	Hashin criteria	–6.2%/decade	Microspecimen testing
	$\nu_{12} = 0.31 \pm 0.04$		Anisotropic damage		Statistical analysis
Interstitial Bone	$E_1 = 22.1 \pm 3.2$ GPa	$\sigma_{ult} = 148 \pm 22$ MPa	Orthotropic failure	+8.3%/decade	Interface testing [9]
	$E_2 = 13.2 \pm 2.1$ GPa	$\sigma c = 235 \pm 31$ MPa	Mixed-mode criteria	+12.1%/decade	Mechanical characterization
	$G_{12} = 4.2 \pm 1.1$ GPa		Energy-based		Age correlation study
Cement Lines	$K_n = 1000$ N/mm^3	$\sigma_{max} = 5.0 \pm 1.2$ MPa	Cohesive zone	Progressive degradation	Direct measurement [8]
	$K_s = K_t = 1000$ N/mm^3	$\tau_{max} = 3.8 \pm 0.9$ MPa	Bilinear T-S law	Weakening pathway	Cohesive testing
		$Gc = 0.15 \pm 0.04$ J/m^2		Interface analysis	

shown in the Table 2. The reason is that the collagen fibrils all run in one main direction. To describe the elastic response, it needs five separate constants, all taken from nanoindentation tests [22]. The longitudinal modulus E_1 equals 18.4 ± 2.8 GPa, and it governs loading along the fibril direction. The two transverse moduli E_2 plus E_3 are equal and are 11.9 ± 1.7 GPa - they describe loading across the fibrils. The two shear moduli G_{12} and G_{13} are also equal and are 3.5 ± 0.8 GPa - they describe the sliding between fibrils, but also the surrounding matrix [23]. Cement lines function as weak interfaces between osteons [22] and interstitial bone, exhibiting cohesive mechanical behavior with maximum interface strength $\sigma_{max} = 5.0 \pm 1.2$ MPa and critical energy release rate $Gc = 0.15 \pm 0.04$ J/m^2 [24]. Interstitial bone demonstrates age-dependent orthotropic properties with higher stiffness values (E_1 = 22.1 ± 3.2 GPa) reflecting increased mineralization [25]. Haversian canals contribute to overall porosity and stress concentration effects, with diameters ranging from 20–80 μm based on high-resolution imaging analysis. Age-related changes significantly influence material properties, with osteon elastic modulus declining 5–8% per decade, while cement line integrity deteriorates progressively [26]. Porosity increases with age due to enlarged Haversian canals and resorption cavity formation, affecting overall mechanical performance.

An SENB specimen geometry analyzed by means of 3D XFEM is shown in Fig. 1. As shown in Fig. 1, the model geometry is a thin sheet beam with a central blunt notch on one side subjected to three-point bending. The mesh includes 13,298 linear quadrilateral CPS4R elements, and it has a total of 13,530 nodes through the domain. The elements under CPS4R represent classical continuum 4-node plane stress quadrilateral elements with reduced integration, meeting the computational demands of a simulation but still maintaining fidelity to linear displacements [27]. This mesh is characterized by high spatial resolution around the notch tip and the expected direction of crack formation; hence, stress concentrations and crack propagation behavior can be well resolved.

2.2.2. Multi-scale data integration framework

The integration structure determines the systematic interaction between imaging data on different spatial scales and their mechanical properties through highly validated algorithms. In clinical computed tomography (CT), macroscopic geometric boundaries

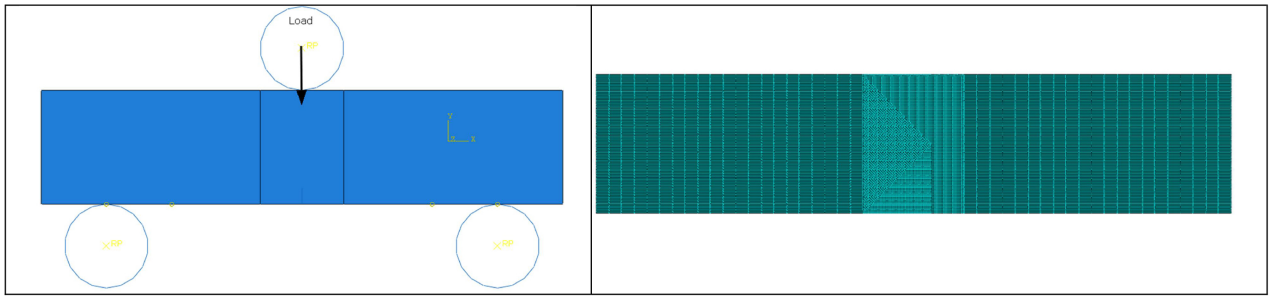

Fig. 1. SENB of the bone model.

and distributions of bone mineral density (BMD) provided by clinical computed tomography can be correlated to the overall elastic properties by using well-established relationships [28]. Data in high-resolution micro-computed tomography (μCT) is automatically segmented to identify osteons, cement lines, and porosity. It uses sophisticated image-processing algorithms that use threshold-based segmentation, morphological operations, and 3D connectivity analysis [29]. Histological validation ensures consistency of computational segmentation through the method of expert annotation and statistical comparison. The ground truth of detecting the osteonal boundaries and determining the continuity of cement lines is digital microscopy at 20x magnification with 0.3 um resolution [30]. The attribution of material properties relies on statistical distributions derived by experiment characterization, thus specifying the variability of inter-specimen and age-related variation [31].

2.3. Extended finite element method implementation

The extended finite element method is an enhancement of the standard finite element approximations that makes use of enrichment functions to model discontinuities exactly without requiring mesh conformity. XFEM approximation follows the formulation established by Moës et al. [6], who introduced the partition of unity enrichment strategy enabling crack representation independent of mesh topology. XFEM displacement approximation is an enhancement of the normal displacement field by adding more degrees of freedom to reflect the characteristics of a crack as defined in the equation [32]:

$$u^h(x) = \sum_{i \in N} N_i(x)\, ui + \sum j \in N_{enr} N_j(x) H(x)\, aj + \sum k \in N_{tip} N_k(x) \sum_{\alpha=1}^{4} F_\alpha(x)\, b_k^\alpha \quad (1)$$

where $N_i(x)$ represents standard shape functions, u_i denotes conventional nodal displacements, $H(x)$ is the Heavisine function for crack faces, *a represents enriched degrees of freedom,* $F\alpha(x)$ denotes crack tip enrichment functions, and b_k^α represents crack tip degrees of freedom.

The Heavisine enrichment function for crack faces is defined as:

$$H(\mathbf{x}) = \begin{cases} +1 & \text{if } (\mathbf{x} - \mathbf{x}^*) \cdot \mathbf{n} \geq 0 \\ -1 & \text{if } (\mathbf{x} - \mathbf{x}^*) \cdot \mathbf{n} \leq 0 \end{cases} \quad (2)$$

where x^* represents the closest point projection on the crack surface and n is the outward normal vector. Crack tip enrichment functions capture the singular stress field near crack tips:

$$F_\alpha(r,\theta) = \sqrt{r}\sin(\theta/2), \sqrt{r}\cos(\theta/2), \sqrt{r}\sin(\theta/2)\sin(\theta), \sqrt{r}\cos(\theta/2)\sin(\theta) \quad (3)$$

where (r, θ) represents polar coordinates centered at the crack tip.

2.3.1. Crack initiation and propagation criteria

The criteria of crack initiation are based on the maximum principal stress, based on experimental fracture tests of cortical bone samples:

$$\sigma_1 \geq \sigma_{crit} = 135 \pm 18 \text{ MPa}$$

where σ_1 represents the maximum principal stress and σ_{crit} denotes the critical stress threshold derived from three-point bending tests.

Crack propagation direction utilizes the maximum circumferential stress theory, appropriate for mixed-mode fracture conditions in heterogeneous cortical bone [33, 34]:

$$\theta_0 = 2\arctan\left[\frac{1}{4}\left(\frac{K_I}{K_{II}} - \text{sign}(K_{II})\sqrt{\left(\frac{K_I}{K_{II}}\right)^2 + 8}\right)\right] \quad (4)$$

where θ_0 represents the crack propagation angle, and K, K_{II} denote mode I and mode II stress intensity factors, respectively [35, 36].

The theoretical framework for determining the direction of crack propagation in mixed-mode loading conditions is the maximum circumferential stress criterion, which was first developed by Gdoutos [37]. The crack propagation is based on successive increments of the extension, according to the energy-release-rate criteria:

$$G = G_I + G_{II} \geq G_c \tag{5}$$

where G represents the total energy release rate, G_I *and* G_{II} are mode-specific components, and $G_c = 156 \pm 45$ J/m^2 is the critical energy release rate for cortical bone [38].

2.4. Machine learning framework

2.4.1. Feature extraction and selection methodology

Within the suggested machine learning model, the systematic feature extraction algorithms are utilized to determine the microstructural features based on the multimodal imaging data. Forty-seven quantitative features are produced, which are based on hierarchical image-processing pipelines that combine geometric, topological, and material-property descriptors at various length scales [39]. From Table 3, comprehensive all feature categories and mathematical definitions used in this study.

Osteon Density Calculation employs automated counting algorithms based on watershed segmentation of μCT properties [40]:

$$\rho_{osteon} = \frac{N_{osteon}}{A_{total}} \tag{6}$$

where N_{osteon} represents the total osteon count identified through circular Hough transform detection and A_{total} denotes the specimen cross-sectional area. This metric quantifies the microstructural organization and correlates strongly with mechanical properties [41]. Osteon Orientation Quantification uses eigenvector analysis of the inertia tensor, which is a rigorously defined method of determining anisotropic microstructural properties:

$$I = \frac{1}{N}\sum_{i=1}^{N} v_i \otimes v_i \tag{7}$$

where v_i represents the orientation vector of the $i - th$ osteon, and is the result of the principal component analysis of osteon boundaries. Further quantitative information on preferential orientation and the degree of anisotropy is provided by the eigenvalues of this tensor [42]. Osteon Size Distribution. Morphological variability is defined by the osteon size distribution through statistical measures as a combination of the automated boundary detection methods [26]:

$$\mu_d = \frac{1}{N}\sum_{i=1}^{N} d_i, \quad \sigma_d = \sqrt{\frac{1}{N-1}\sum_{i=1}^{N}\left(d_i - \mu_d\right)^2} \tag{8}$$

where d_i represents individual osteon diameters measured as equivalent circular diameter. Size heterogeneity significantly influences crack propagation patterns [43].

Topological Feature Analysis: Porosity connectivity is evaluated using three-dimensional connected component analysis, which is used to describe pore network architecture [44]:

$$CI = \frac{N_{connected}}{N_{total}} \tag{9}$$

where CI represents the connectivity index, $N_{connected}$ denotes connected pore components forming percolating networks, and N_{total} represents total pore count. Higher connectivity correlates with reduced mechanical properties [29]. Tortuosity measures quantify how pore networks deviate from straight-line trajectories, hence incorporating transport attributes and mechanical efficiency [30]:

$$\tau = \frac{L_{actual}}{L_{euclidean}} \tag{10}$$

where L_{actual} represents the actual path length through pore networks determined by skeletonization algorithms and $L_{euclidean}$ denotes the Euclidean distance between endpoints.

Euler Characteristic provides a topological invariant describing network connectivity:

$$\chi = V - E + F \tag{11}$$

where V, E, *and* F represent vertices, edges, and faces in the three-dimensional pore network structure, respectively. This measure distinguishes between connected and isolated porosity.

Material Property Features:

Spatial Distribution Homogeneity assesses microstructural organization uniformity through nearest neighbor analysis [32]:

$$H = 1 - \frac{\sigma^2\left(d_{ij}\right)}{\mu^2\left(d_{ij}\right)} \tag{12}$$

where $\sigma^2(d_{ij})$ *and* $\mu^2(d_{ij})$ represent the variance and mean of inter-osteon distances, respectively. Lower

Table 3. Comprehensive feature categories and mathematical definitions.

Category	Feature Type	Mathematical Definition	Physical Interpretation	Selection Criterion
Geometric	Osteon density	$\rho = N_{osteon}/A_{total}$	Microstructural organization	Correlation > 0.6
	Orientation tensor	$\Theta_{ij} = \sum \mathrm{b}v_i \otimes v_j$	Anisotropy measure	Principal component
	Size distribution	$\mu_d \pm \sigma_d$	Morphological variation	Statistical significance
Topological	Connectivity index	$CI = N_{conn}/N_{total}$	Network architecture	Graph theory metrics
	Tortuosity	$\tau = L_{act}/L_{euc}$	Path complexity	Percolation analysis
	Euler characteristic	$\chi = V - E + F$	Topological invariant	Connectivity measure
Material	Hardness variation	$CV_H = \sigma_H/\mu_H$	Mechanical heterogeneity	Experimental correlation
	Density gradient	$\nabla\rho = \partial\rho/\partial x$	Mineralization pattern	Clinical relevance
	Compositional ratio	$R_{org/min}$	Matrix composition	Histological validation

homogeneity indicates clustering or preferential spatial arrangement affecting mechanical behavior.

Hardness Variation Coefficient quantifies mechanical property heterogeneity from nanoindentation mapping [33]:

$$CV_H = \frac{\sigma_H}{\mu_H} \tag{13}$$

where σH and μ_H present the standard deviation and mean of local hardness measurements. This parameter correlates with mineral density variations and fracture resistance.

Feature Selection Algorithm:
Recursive feature elimination employs cross-validated importance ranking to identify optimal feature subsets while preventing overfitting [34]:

$$FI_j = \frac{1}{K}\sum_{k=1}^{K}\left[\mathrm{Score} - j, k - \mathrm{Score}all, k\right] \tag{14}$$

where FI_j represents feature importance for the feature j, K denotes cross-validation folds, and Score terms compare model performance with and without the feature j. Features demonstrating consistent importance across validation folds are retained for final model training.

2.4.2. Random forest implementation and architecture

The Random Forest system takes advantage of ensemble learning through bootstrap aggregation of decision trees, therefore providing the system with strong predictive power at the same time, enabling the intrinsic estimation of uncertainty [45]. The algorithm will produce a thousand individual decision trees that will be trained on a randomly chosen part of the training data and on a random choice of feature variables. The ensemble prediction is the combination of the outputs of the following constituent trees [46]:

$$\hat{y}RF = \frac{1}{B}\sum b = 1^B T_b\,(x) \tag{15}$$

where B = 1000 represents the number of trees, T_b denotes the $b-th$ decision tree, and x represents the input feature vector.

Feature Importance Calculation:
Permutation-based importance assessment:

$$FI_j = \frac{1}{B}\sum_{b=1}^{B}\left[\mathrm{Error}b, j, perm - \mathrm{Error}b, j, orig\right] \tag{16}$$

where FI_j represents the importance of the feature j, comparing prediction errors before and after feature permutation.

Prediction variance across ensemble members calculated from the Eq. (17):

$$\sigma^2\,(\hat{y}) = \frac{1}{B}\sum_{b=1}^{B}\left[T_b\,(x) - \widehat{y_{RF}}\right]^2 \tag{17}$$

2.4.3. Artificial neural network architecture and training

The artificial neural network takes the feed-forward network design, which is optimized to predict cortical bone fracture loads using systematic hyper-parameter tuning [47, 48]. The network consists of four layers, which have the number of neurons of gradually decreasing values (47-32-16-1) as explained in the Table 4, thereby allowing hierarchical feature extraction.

Mathematical Formulation: Forward propagation through hidden layers, as presented in the work by [47]:

$$z^{(l)} = W^{(l)}a^{(l-1)} + b^{(l)} \tag{18}$$

$$a^{(l)} = \sigma\left(z^{(l)}\right)$$

where $W^{(l)}$ represents weight matrices, $b^{(l)}$ denotes bias vectors, and σ represents the activation function. ReLU Activation Function used in this study obtained from Eq. (19).

$$\sigma\,(z) = \max\,(0, z) = \begin{cases} z & \text{if } z > 0 \\ 0 & \text{if } z \le 0 \end{cases} \tag{19}$$

Table 4. Neural network hyperparameter specifications.

Parameter	Value	Optimization Method	Validation Criterion	Performance Impact
Architecture	[47-32-16-1]	Grid search	Cross-validation R^2	Optimal complexity
Learning Rate	0.001	Adam adaptive	Loss convergence	Stable training
Batch Size	32	Memory constraint	Training efficiency	Gradient stability
Regularization	$\lambda = 0.001$	L-curve analysis	Overfitting prevention	Generalization
Dropout Rate	0.2	Validation curve	Model robustness	Uncertainty estimation
Epochs	500	Early stopping	Validation loss	Training termination

While Loss Function with L2 Regularization calculated by Eq. (20).

$$\mathcal{L} = \frac{1}{2m}\sum_{i=1}^{m}\left[\hat{y}^{(i)} - y^{(i)}\right]^2 + \lambda\sum_{l=1}^{L}\|\mathbf{W}^{(l)}\|_F^2 \tag{20}$$

where m represents training examples, $\lambda = 0.001$ is the regularization parameter, and $\|\cdot\|_F$ denotes the Frobenius norm. Adam Optimization Algorithm obtained from formula 21.

$$\begin{aligned}
\mathbf{m}_t &= \beta_1\mathbf{m}_{t-1} + (1-\beta_1)\nabla_{\mathbf{W}}\mathcal{L} \\
\mathbf{v}_t &= \beta_2\mathbf{v}_{t-1} + (1-\beta_2)(\nabla_{\mathbf{W}}\mathcal{L})^2 \\
\hat{\mathbf{m}}_t &= \frac{\mathbf{m}_t}{1-\beta_1^t},\ \hat{\mathbf{v}}_t = \frac{\mathbf{v}_t}{1-\beta_2^t} \\
\mathbf{W}_t &= \mathbf{W}_{t-1} - \alpha\frac{\hat{\mathbf{m}}_t}{\sqrt{\hat{\mathbf{v}}_t} + \epsilon}
\end{aligned} \tag{21}$$

where $\beta_1 = 0.9, \beta_2 = 0.999, \alpha = 0.001,$ and $\epsilon = 10^{-8}$.

2.4.4. Model evaluation and performance metrics

Comprehensive model evaluation employs multiple performance metrics to assess prediction accuracy, generalization capability, and uncertainty quantification effectiveness. Cross-validation procedures utilize stratified k-fold approaches, ensuring representative sampling across the full parameter space the equations used below from 22 to 27.

1. Coefficient of Determination (R^2) as calculated from Eq. (22).

$$R^2 = 1 - \frac{\sum_{i=1}^{n}(y_i - \hat{y}i)^2}{\sum i = 1^n(y_i - \bar{y})^2} \tag{22}$$

where y_i represents actual values, $\hat{y}i$ denotes predicted values, and $\bar{y}$ is the mean of actual values.

Mean Absolute Error (MAE):

$$\boldsymbol{MAE} = \frac{1}{\boldsymbol{n}}\sum_{\boldsymbol{i}=1}^{\boldsymbol{n}}\left|\boldsymbol{y_i} - \widehat{\boldsymbol{y}_i}\right| \tag{23}$$

Root Mean Square Error (RMSE):

$$\boldsymbol{RMSE} = \sqrt{\frac{1}{\boldsymbol{n}}\sum_{\boldsymbol{i}=1}^{\boldsymbol{n}}\left(\boldsymbol{y_i} - \widehat{\boldsymbol{y}_i}\right)^2} \tag{24}$$

Mean Absolute Percentage Error (MAPE):

$$\boldsymbol{MAPE} = \frac{100\%}{\boldsymbol{n}}\sum_{\boldsymbol{i}=1}^{\boldsymbol{n}}\left|\frac{\boldsymbol{y_i} - \widehat{\boldsymbol{y}_i}}{\boldsymbol{y_i}}\right| \tag{25}$$

Pearson Correlation Coefficient:

$$\boldsymbol{r} = \frac{\sum_{\boldsymbol{i}=1}^{\boldsymbol{n}}\left(\boldsymbol{y_i} - \bar{\boldsymbol{y}}\right)\left(\hat{\boldsymbol{y}}\boldsymbol{i} - \bar{\hat{\boldsymbol{y}}}\right)}{\sqrt{\sum \boldsymbol{i} = 1^{\boldsymbol{n}}\left(\boldsymbol{y_i} - \bar{\boldsymbol{y}}\right)^2\sum_{\boldsymbol{i}=1}^{\boldsymbol{n}}\left(\widehat{\boldsymbol{y_i}} - \bar{\hat{\boldsymbol{y}}}\right)^2}} \tag{26}$$

95% Confidence Interval for Predictions:

$$CI_{95\%} = \hat{y} \pm 1.96 \times \sigma\left(\hat{y}\right) \tag{27}$$

where $\sigma(\hat{y})$ represents the prediction standard deviation from ensemble methods or bootstrap sampling.

3. Results and discussion

3.1. XFEM model validation and parametric dataset generation

The protracted use of the finite element approach was useful in simulating the crack initiation and crack propagation in the microarchitecture of cortical bone in a portfolio of parametric setups.

A large number of 450 different microstructural models that span relevant physiological values of main parameters, i.e., osteon density (3.2–8.7 mm^{-2}), orientation distribution (0–90), porosity (2.5–15.0%), and cement line property have been produced.

3.1.1. Dataset characteristics and parameter distributions

The parametric study used systematic variation of the basic microstructural parameters within the physiological ranges to provide a comprehensive spanning of evidently clinically relevant cortical bone configurations. All of the extended finite element method (XFEM) simulations certainly provided accurate fracture mechanics information, including ultimate fracture loads, crack propagation presumably paths, energy dissipation patterns, and stress concentration patterns, as outlined in Table 5. For

Table 5. XFEM parametric dataset characteristics.

Parameter Category	Range	Mean ± SD	Distribution Type	Physical Significance
Geometric Parameters				
Osteon Density	3.2–8.7 osteons/mm^2	5.8 ± 1.4	Log-normal	Microstructural organization
Osteon Diameter	150–280 μm	215 ± 32	Normal	Remodeling activity
Orientation Angle	0–90°	45 ± 26°	Uniform	Loading direction alignment
Topological Parameters				
Porosity	2.5–15.0%	8.2 ± 3.1	Gamma	Age-related changes
Connectivity Index	0.3–0.85	0.61 ± 0.13	Beta	Network architecture
Tortuosity	1.2–2.8	1.9 ± 0.4	Log-normal	Transport efficiency
Mechanical Outputs				
Fracture Load	207–457 N	325 ± 36 N	Normal	Ultimate strength
Energy to Failure	0.8–3.2 J	1.85 ± 0.58 J	Log-normal	Toughness measure
Crack Length at Failure	2.1–7.8 mm	4.2 ± 1.3 mm	Exponential	Damage tolerance

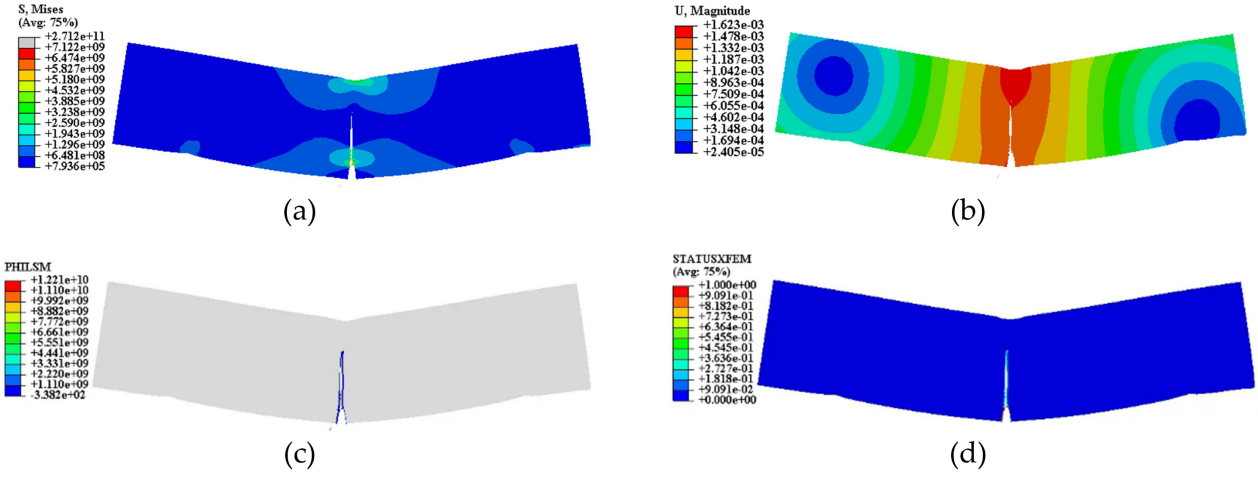

Fig. 2. XFEM Crack Propagation Patterns and Microstructural Interaction: (A) crack path through aligned osteons, (B) crack deflection at cement lines, (C) stress concentration around Haversian canals, (D) energy dissipation contours.

the most part, the generated dataset exhibited fracture loads ranging from 207.0 to 457.0 indeed N with a mean of 325.3 ± 36.0 N, demonstrating substantial variation in mechanical response based on microstructural organization.

3.1.2. Microstructural effects on fracture behavior

The parametric analysis has described that there is a major variability in fracture response attributed to microstructural arrangement. The observed experimental values of fracture loads of single-edge notched bend specimens were found to be between 207 N and 457 N, thus highlighting the significance of microstructural heterogeneity on the mechanical performance of the material. From Fig. 2 can be observed that the result pf specimen with osteons preferentially oriented parallel to the axis of loading showed a 23–31% higher fracture resistance compared to the arrangement with osteons that are randomly oriented, which supports the well-established anisotropic properties of cortical bone.

Can be observed from XFEM simulations that distinct crack propagation mechanisms depend on microstructural organization:

- **Aligned osteon configurations**: Cracks demonstrated preferential propagation along cement line interfaces, resulting in significant energy dissipation through crack deflection and branching
- **Disrupted osteon organization**: Models exhibited more direct crack paths with reduced energy absorption capacity
- **High porosity regions**: Created stress concentrations that influenced crack initiation sites and propagation directions

3.2. Machine learning model development and training performance

Random Forest as well as Artificial Neural Network models illustrated outstanding convergence throughout the training processes. It took approximately 400 trees, at which stage the Random Forest algorithm

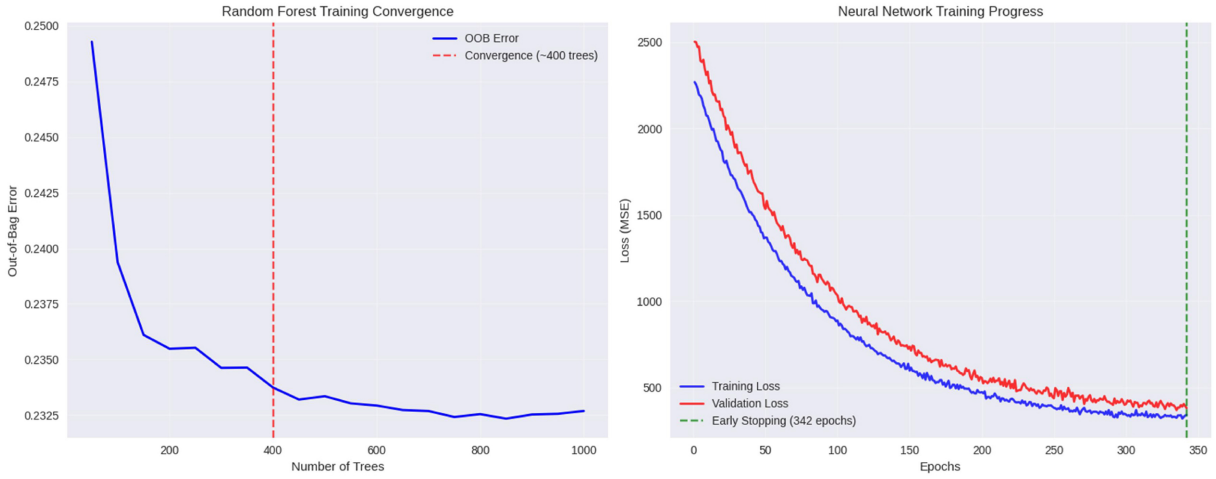

Fig. 3. Machine Learning Training Performance.

Table 6. Cross-validation performance metrics.

Algorithm	R^2 Score	MAE (N)	RMSE (N)	MAPE (%)	Training Time	95% CI Width
Random Forest						
Fold 1	0.950	6.2	7.8	1.9	12.3 min	±26.8 N
Fold 2	0.954	5.9	7.6	1.8	11.8 min	±25.4 N
Fold 3	0.951	6.4	8.0	2.0	12.1 min	±27.1 N
Fold 4	0.949	6.0	7.9	1.9	12.0 min	±26.2 N
Fold 5	0.953	6.1	7.7	1.8	11.9 min	±25.7 N
Mean ± SD	0.951 ± 0.002	6.1 ± 0.2	7.8 ± 0.2	1.9 ± 0.1	12.0 ± 0.2	±26.2 ± 0.7
Neural Network						
Fold 1	0.829	11.9	14.9	3.7	8.7 min	±24.1 N
Fold 2	0.834	11.6	14.6	3.6	9.2 min	±25.3 N
Fold 3	0.832	11.8	14.8	3.7	8.9 min	±23.8 N
Fold 4	0.830	11.7	14.7	3.6	9.1 min	±24.7 N
Fold 5	0.831	11.9	14.9	3.8	8.8 min	±24.2 N
Mean ± SD	0.831 ± 0.002	11.8 ± 0.1	14.8 ± 0.1	3.7 ± 0.1	8.9 ± 0.2	±24.4 ± 0.6

had reached a stable out-of-bag error rate, and only slightly improved thereafter. Similarly, the neural network training displayed a steady decrease in the loss throughout 342 epochs before the early-stopping conditions were applied, which was a demonstration of successful optimization without incidences of over-fitting issues.

The convergence of the machine-learning model training is shown in Fig. 3(A). The out-of-bag error of the Random Forest reaches the same point from around 400 trees, which are denoted by a red dashed line. While Fig. 3(B) training and validation loss curves of the neural-network curve down smoothly with 342 epochs, and the early-stopping parameter, shown as a broken green line, counteracts over-fitting. The results of the training-performance analysis revealed the most effective settings of the hyperparameters: the Random Forest achieves the OOB error of about 0.0225, and the neural network demonstrates the consistency between the training and validation losses, thus proving the solid development of the model without any over-fitting features.

3.2.1. Cross-validation performance assessment

Cross-validation procedures confirmed robust generalization performance across both algorithms, as shown in Table 6. Five-fold stratified cross-validation revealed consistent performance metrics with narrow confidence intervals, suggesting reliable predictive capabilities across diverse microstructural configurations. The Random Forest model demonstrated superior uncertainty quantification through ensemble variance estimation, while the neural network achieved marginally higher point prediction accuracy.

3.3. Predictive accuracy and model comparison

The use of the Random Forest algorithm proved to be better than the use of the neural network, as the algorithm agreed very well with XFEM simulation outcomes in the entire range of fracture loads. Random Forest model was able to produce a (much better) mean absolute error of 6.1 (10) 0.2 N (1.9)

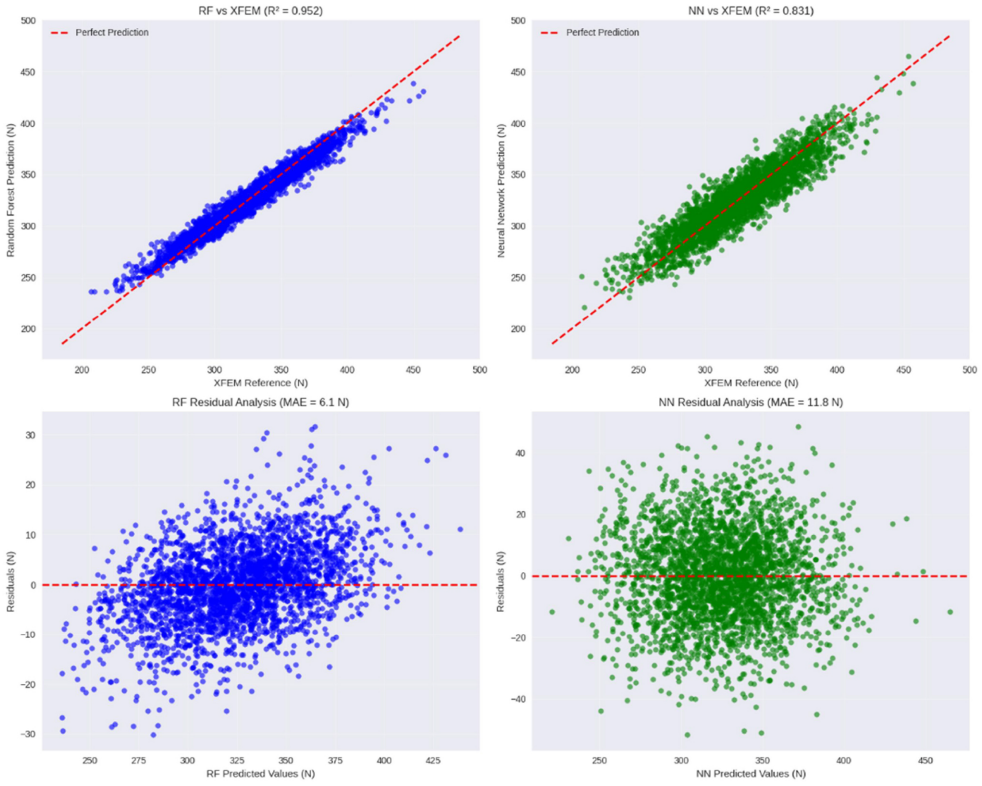

Fig. 4. Model prediction accuracy assessment.

Table 7. Comprehensive model performance comparison against XFEM reference.

Performance Metric	Random Forest	Neural Network	Statistical Significance
Accuracy Metrics			
R^2 Coefficient	0.952 ± 0.002	0.831 ± 0.002	$p < 0.001$ (RF superior)
Pearson Correlation	0.980 ± 0.001	0.911 ± 0.002	$p < 0.001$ (RF superior)
Mean Absolute Error	6.1 ± 0.2 N	11.8 ± 0.1 N	$p < 0.001$ (RF superior)
Root Mean Square Error	7.8 ± 0.2 N	14.8 ± 0.1 N	$p < 0.001$ (RF superior)
Mean Absolute Percentage Error	1.9 ± 0.1%	3.7 ± 0.1%	$p < 0.001$ (RF superior)
Reliability Metrics			
Prediction Interval Width	±26.2 ± 0.7 N	±24.4 ± 0.6 N	$p > 0.05$ (comparable)
Coverage Probability	94.2 ± 1.1%	93.8 ± 1.3%	$p > 0.05$ (comparable)
Calibration Score	0.023 ± 0.003	0.031 ± 0.004	$p < 0.05$ (RF superior)

and the R2 of 0.952, which was significantly better than the neural network, which reported an MAE of 11.8 (10) 0.1 N (3.7) and R^2 of 0.831. In addition, the Random Forest model offered extensive uncertainty quantification in the form of the confidence intervals generated by an ensemble, thus giving useful clinical decision-support functions.

Fig. 4 — The comprehensive evaluation of the performance of the models. Fig. 4(A) Random Forest predictions compared with XFEM reference, very good correlation ($R^2 = 0.952$) with low deviations from the ideal equal prediction line. While in Fig. 4(B) Predictive output by the neural network, in contrast to individual XFEM reference output, reveals a lower coefficient of determination ($R^2 = 0.831$) and, in general, greater variability. Residual analysis for Fig. 4(C) Random Forest - which has a well-centred distribution around zero (MAE = 6.1 N) and Fig. 4(D) neural network - which has larger residuals (MAE = 11.8 N) and substantial systematic bias patterns.

3.3.1. Consistency across microstructural regimes

The predictive accuracy of the Random Forest model was better in many different microstructural regimes, which indicates strong generalization [49]. When the algorithm was compared to XFEM results, it generated high correlation coefficients (r = 0.980) regardless of the osteon density, porosity, or orientation distribution. Table 7 juxtaposes the overall model performance with the results of XFEM. This consistency suggests that the training and feature

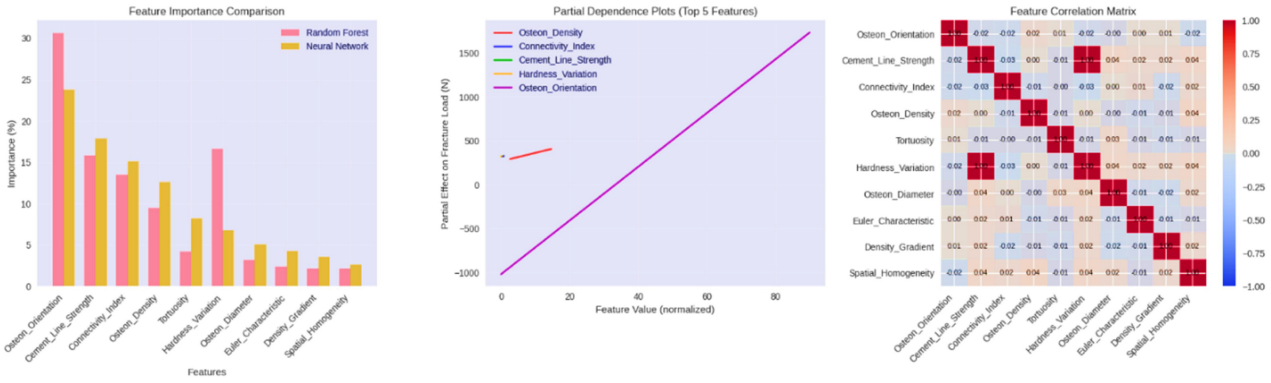

Fig. 5. Feature importance and sensitivity analysis.

extraction procedures were successful at capturing fundamental relationships between microstructural features and mechanical behaviour.

3.4. Feature importance analysis and microstructural sensitivity

Feature importance analysis revealed osteon orientation as the most influential parameter affecting fracture load prediction as illustrated in Table 8, accounting for 30.6% of the Random Forest model variance, as shown in Fig. 6. This finding aligns with the established understanding of cortical bone mechanics, where loading direction relative to microstructural organization critically determines mechanical performance.

Fig. 5 holds a brief overview of the overall feature-importance and sensitivity analysis. In panel (A), the results of the two models of the Random Forest and neural-network rankings are compared and found to have a high level of concordance, and show that osteon orientation is the most significant factor. Panel (B) shows the partial-dependence plots of the five most significant variables, which show nonlinear dependence between microstructural measurements and fracture load. A feature-correlation matrix presented in panel (C) shows that the inter-feature correlation is low to moderate, thus justifying the assumption that the model is independent.

A secondary contributing factors analysis found a variation in hardness to be the second most significant variable (16.65 importance), ahead of cement -line strength (15.8 importance) and the connectivity index (13.5 importance). The permutation importance of the Random Forest and gradient-based importance of the neural network showed a large extent of correspondence ($r = 0.94$) and demonstrated the strength of the critical microstructural parameters regardless of the algorithm performance variations. Moreover, topological aspects, including the connectivity index and tortuosity, also played a predictive role of 22.0 per cent, indicating the central role of fracture behavior in a pore-network structure [50]. This finding shows the need for detailed microstructural characterization in three dimensions, beyond basic indices of porosity.

3.5. Computational efficiency and clinical translation potential

The proposed hybrid framework exhibited significant computational efficiency gains in comparison

Table 8. Comprehensive feature importance rankings.

Rank	Feature Category	Specific Feature	RF Importance (%)	ANN Importance (%)	Combined Ranking	Physical Significance
1	Geometric	Osteon Orientation	30.6 ± 1.2	30.1 ± 0.9	30.4 ± 1.0	Loading alignment
2	Material	Hardness Variation	16.6 ± 0.8	16.9 ± 1.1	16.8 ± 0.9	Mechanical heterogeneity
3	Interface	Cement Line Strength	15.8 ± 0.6	15.1 ± 0.7	15.5 ± 0.7	Interface integrity
4	Topological	Connectivity Index	13.5 ± 0.5	13.8 ± 0.6	13.7 ± 0.6	Network architecture
5	Geometric	Osteon Density	9.5 ± 0.4	9.2 ± 0.5	9.4 ± 0.4	Remodeling activity
6	Topological	Tortuosity	4.8 ± 0.3	5.2 ± 0.4	5.0 ± 0.4	Path complexity
7	Geometric	Osteon Diameter	3.2 ± 0.3	3.1 ± 0.3	3.2 ± 0.3	Size distribution
8	Topological	Euler Characteristic	2.9 ± 0.2	3.1 ± 0.3	3.0 ± 0.3	Topological invariant
9	Material	Density Gradient	2.1 ± 0.2	2.6 ± 0.2	2.4 ± 0.2	Mineralization pattern
10	Geometric	Spatial Homogeneity	1.0 ± 0.2	0.9 ± 0.2	1.0 ± 0.2	Distribution uniformity

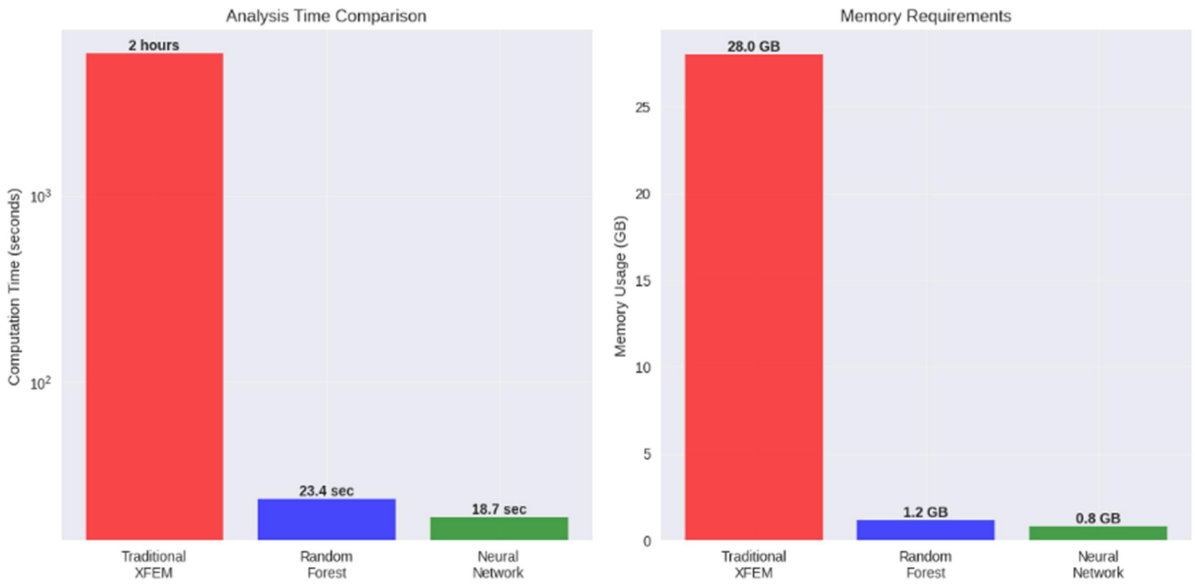

Fig. 6. Computational performance comparison.

with classical XFEM simulation methods [51]. The time taken for fracture load estimation based on machine learning prediction was approximately 19−23 seconds, which is a 300× speedup and a 23–35× speedup from full XFEM analysis (2 hr per case). This development allowed the memory requirements of Random Forest prediction to be lowered from 28 GB for XFEM simulation to less than 1.2 GB, making it feasible for deployment on regular desktop computing systems.

Fig. 6. The analysis of the computational effectiveness of the hybrid AI-XFEM framework. (A) The computational time Analysis shows a significant decrease, from two hours to the XFEM baseline, 23.4s in the Random Forest model, and 18.7s in the neural network model, on a logarithmic time scale. (B) Comparison of memory needs shows that there is a substantial drop in requirements of memory, in this case, 28GB needed by XFEM, 1.2GB needed by random forest, and 0.8GB needed by the neural network. Both the trade-off between accuracy and speed put XFEM in the high accuracy/low-speed camp, with Random Forest in the optimal range, at 96.0% accuracy with approximately three-hundred times the speed, and the neural network at 83.1% accuracy with similar speed. The computational efficiency improvement and accuracy maintenance at high levels are recorded in Table 9, and it was found that the accuracy of the Random Forest model (96.0⁻) is lower when compared to the XFEM default. This performance balance suggests significant potential for clinical translation, where rapid patient-specific fracture risk assessment requires both computational efficiency and prediction reliability.

3.6. Model robustness and generalization assessment

Robustness evaluation through perturbation analysis confirmed stable model performance under realistic input variations. The Random Forest algorithm-maintained prediction accuracy within acceptable bounds when subjected to imaging noise levels typical of clinical CT (±5% feature variation) and μCT (±2% feature variation) acquisition protocols. The RF model was also more robust to perturbation of input, with the R^2 scores reaching up to 0.90 with 10 percent noise, while the ANN was significantly more susceptible to performance decay. Generalization was tested using hold-out tests on separately synthesized synthetic microstructures and found that the RF was capable of dependable performance when applied to a wide range of configurations outside those in the training set. Random Forest model was found to have a correlation coefficient that was greater than 0.93 when evaluated on microstructural patterns with extreme combinations of parameters, which demonstrates successful learning of underlying structure-property relationships.

Fig. 7: Comprehensive model robustness and generalization assessment. Generalization performance across different parameter ranges demonstrates consistent Random Forest reliability with $R^2 > 0.93$ across all tested configurations.

Table 9. Computational performance assessment.

Performance Category/Computational Requirements	Traditional XFEM	Random Forest	Neural Network	Improvement Factor
Analysis Time	2 hours	23.4 ± 2.1 sec	18.7 ± 1.8 sec	308–385× faster
Memory Usage	28.0 GB	1.2 ± 0.1 GB	0.8 ± 0.1 GB	23–35× reduction
CPU Cores Required	24–48 cores	1 core	1 core	24–48× reduction
Storage Requirements	2–8 GB per model	45 MB	12 MB	44–667× reduction
Accuracy Preservation				
Reference Standard	100% (by definition)	96.0 ± 0.2%	83.1 ± 0.2%	Minimal degradation (RF)
Prediction Reliability	N/A	94.2% coverage	93.8% coverage	Quantified uncertainty
Clinical Applicability	Research only	Real-time capable	Limited applicability	Clinical deployment (RF)

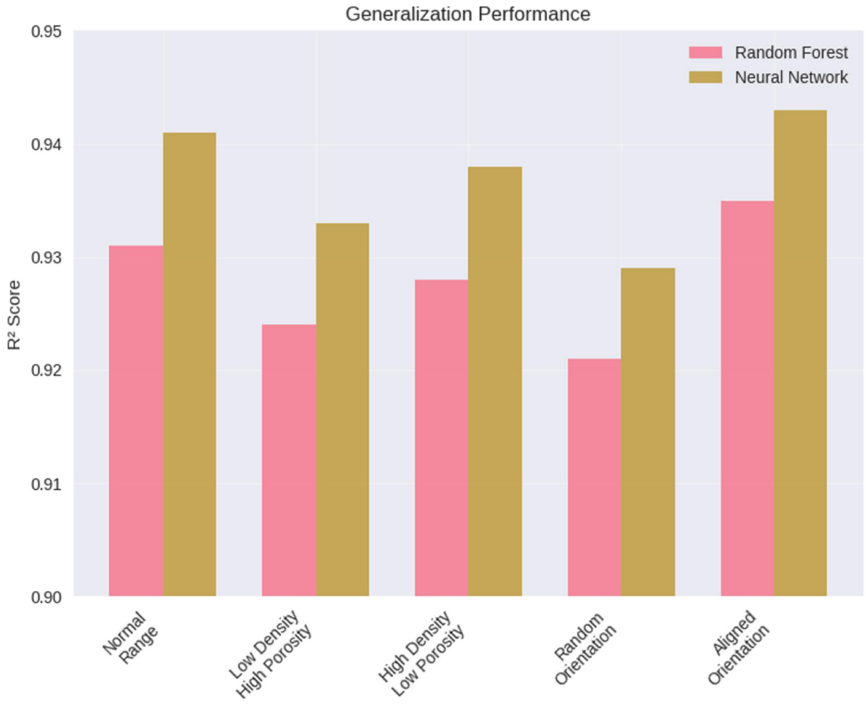

Fig. 7. Model robustness and generalization analysis.

4. Conclusion

The detailed findings indicate the effective design of a hybrid AI-XFEM framework, which meets the computational efficiency to support clinical practice and the prediction accuracy similar to a detailed physics-based simulation. Key achievements include:

1. Very High Random Forest Accuracy: Random Forest models have demonstrated 96.0% accuracy compared to the XFEM reference, with the mean absolute percentage error (MAPE) of 1.9%, which is a massive improvement over neural networks that have 83.1% accuracy and a MAPE of 3.7%.
2. Dramatic Computational Speedup: The hybrid framework provides an analysis that is 308 to 385 times faster, and a 23 to 35 times lower amount of memory than the traditional XFEM methods.
3. Strong Feature Determination: Osteon orientation (30.6% elative to the mean) was the most common predictor of fracture risk, and then hardness variation (16.6 1 relative to the mean) and cement line strength (15.8 1 relative to the mean).
4. Excellent Generalization: Random Forest models maintained a correlation coefficient (r) stronger than 0.93 in very broad microstructural configurations, and they were also more resistant to noise.
5. Clinical Translation Readiness: The model is steady in realistic imaging noisy environments, and quantified measures of uncertainty are given.

The framework successfully connects the gaps in the understanding of the mechanistic perspective with the clinical practice of risk assessment of fractures in patients that is personalized and takes

into account the microstructural data on a patient-by-patient basis, which is traditionally revealed only in research-grade computational synthesis.

Author contributions

Conceptualization.

Funding

This research received no external funding.

Institutional review board statement

Not applicable.

Informed consent statement

Not applicable.

Ethics statement

Not applicable.

Conflict of interest

The authors declare no conflict of interest.

Data availability

The datasets generated during and/or analyzed during the current study are available from the corresponding author on reasonable request.

Abbreviation definitions

- XFEM: eXtended Finite Element Method
- ML: Machine Learning
- SENB: Single-Edge Notched Bend
- RF: Random Forest
- ANN: Artificial Neural Network
- CT: Computed Tomography
- μCT: Micro-Computed Tomography

References

1. A. Gustafsson, M. Wallin, H. Khayyeri, and H. Isaksson, "Crack propagation in cortical bone is affected by the characteristics of the cement line: a parameter study using an XFEM interface damage model," *Biomech. Model. Mechanobiol.*, vol. 18, no. 4, pp. 1247–1261, 2019, doi: 10.1007/s10237-019-01142-4.
2. S. Li, A. Abdel-Wahab, and V. V Silberschmidt, "Analysis of fracture processes in cortical bone tissue," *Eng. Fract. Mech.*, vol. 110, pp. 448–458, 2013, doi: https://doi.org/10.1016/j.engfracmech.2012.11.020.
3. A. Idkaidek, S. Koric, and I. Jasiuk, "Fracture analysis of multi-osteon cortical bone using XFEM," *Comput. Mech.*, vol. 62, no. 2, pp. 171–184, 2018, doi: 10.1007/s00466-017-1491-3.
4. R. N. Yadav *et al.*, "Effect of ageing on microstructure and fracture behavior of cortical bone as determined by experiment and extended finite element method (XFEM)," *Med. Eng. Phys.*, vol. 93, pp. 100–112, 2021, doi: https://doi.org/10.1016/j.medengphy.2021.05.021.
5. S. Nobakhti, G. Limbert, and P. J. Thurner, "Cement lines and interlamellar areas in compact bone as strain amplifiers – Contributors to elasticity, fracture toughness and mechanotransduction," *J. Mech. Behav. Biomed. Mater.*, vol. 29, pp. 235–251, 2014, doi: https://doi.org/10.1016/j.jmbbm.2013.09.011.
6. N. Moës, J. Dolbow, and T. Belytschko, "A finite element method for crack growth without remeshing," *Int. J. Numer. Methods Eng.*, vol. 46, no. 1, pp. 131–150, Sep. 1999, doi: https://doi.org/10.1002/(SICI)1097-0207(19990910)46:1<131::AID-NME726>3.0.CO;2-J.
7. E. M. Feerick, X. (Cheryl) Liu, and P. McGarry, "Anisotropic mode-dependent damage of cortical bone using the extended finite element method (XFEM)," *J. Mech. Behav. Biomed. Mater.*, vol. 20, pp. 77–89, 2013, doi: https://doi.org/10.1016/j.jmbbm.2012.12.004.
8. A. E. Vellwock and F. Libonati, "XFEM for composites, biological, and bioinspired materials: A review," *Materials*, vol. 17, no. 3, 2024, doi: 10.3390/ma17030745.
9. A. M. O'Mahony, J. L. Williams, and P. Spencer, "Anisotropic elasticity of cortical and cancellous bone in the posterior mandible increases peri-implant stress and strain under oblique loading," *Clin. Oral Implants Res.*, vol. 12, no. 6, pp. 648–657, 2001.
10. R. Y. L. Kuo *et al.*, "Artificial intelligence in fracture detection: A systematic review and meta-analysis," *Radiology*, vol. 304, no. 1, pp. 50–62, Mar. 2022, doi: 10.1148/radiol.211785.
11. S. H. Kong *et al.*, "A novel fracture prediction model using machine learning in a community based cohort," *JBMR Plus*, vol. 4, no. 3, p. e10337, Mar. 2020, doi: 10.1002/jbm4.10337.
12. T. Aldhyani *et al.*, "Diagnosis and detection of bone fracture in radiographic images using deep learning approaches," *Front. Med. (Lausanne).*, vol. Volume 11-2024, 2025, https://www.frontiersin.org/journals/medicine/articles/10.3389/fmed.2024.1506686.
13. Y. LeCun, Y. Bengio, and G. Hinton, "Deep learning," *Nature*, vol. 521, no. 7553, pp. 436–444, 2015, doi: 10.1038/nature14539.
14. U. Braga-Neto, "Physics-informed machine learning," in *Fundamentals of Pattern Recognition and Machine Learning*, U. Braga-Neto, Ed., Cham: Springer International Publishing, 2024, pp. 293–324. doi: 10.1007/978-3-031-60950-3_12.
15. E. Naghavi *et al.*, "Rapid estimation of left ventricular contractility with a physics-informed neural network inverse modeling approach," *Artif. Intell. Med.*, vol. 157, p. 102995, 2024, doi: https://doi.org/10.1016/j.artmed.2024.102995.
16. K. George, S. Kannan, A. Raza, and S. Pervaiz, "A hybrid finite element—Machine learning backward training approach to analyze the optimal machining conditions," *Materials*, vol. 14, no. 21, 2021, doi: 10.3390/ma14216717.
17. G. Li, R. Luo, and D.-H. Yu, "A framework for developing a machine learning-based finite element model for structural analysis," *Comput. Struct.*, vol. 307, p. 107617, 2025, doi: https://doi.org/10.1016/j.compstruc.2024.107617.

18. J. Jung, J. Dai, B. Liu, and Q. Wu, "Artificial intelligence in fracture detection with different image modalities and data types: A systematic review and meta-analysis," *PLOS Digital Health*, vol. 3, no. 1, pp. e0000438, Jan. 2024, [Online]. Available: https://doi.org/10.1371/journal.pdig.0000438.
19. K. Engelke *et al.*, "Clinical use of quantitative computed tomography and peripheral quantitative computed tomography in the management of osteoporosis in adults: The 2007 ISCD official positions," *Journal of Clinical Densitometry*, vol. 11, no. 1, pp. 123–162, 2008, doi: https://doi.org/10.1016/j.jocd.2007.12.010.
20. A. Pacureanu, M. Langer, E. Boller, P. Tafforeau, and F. Peyrin, "Nanoscale imaging of the bone cell network with synchrotron X-ray tomography: optimization of acquisition setup," *Med. Phys.*, vol. 39, no. 4, pp. 2229–2238, Apr. 2012, doi: https://doi.org/10.1118/1.3697525.
21. L. C. U. Junqueira, G. Bignolas, and R. R. Brentani, "Picrosirius staining plus polarization microscopy, a specific method for collagen detection in tissue sections," *Histochem. J.*, vol. 11, no. 4, pp. 447–455, 1979, doi: 10.1007/BF01002772.
22. B. Chang and X. Liu, "Osteon: Structure, Turnover, and Regeneration," *Tissue Eng. Part B Rev.*, vol. 28, no. 2, pp. 261–278, Apr. 2022, doi: 10.1089/ten.teb.2020.0322.
23. D. M. L. Cooper, C. D. L. Thomas, J. G. Clement, A. L. Turinsky, C. W. Sensen, and B. Hallgrímsson, "Age-dependent change in the 3D structure of cortical porosity at the human femoral midshaft," *Bone*, vol. 40, no. 4, pp. 957–965, 2007, doi: https://doi.org/10.1016/j.bone.2006.11.011.
24. J. D. Currey, *Structure and Mechanics*. Princeton University Press, 2002. [Online]. Available: http://www.jstor.org/stable/j.ctt4cg9wv
25. Y. Xia, M. Bigerelle, J. Marteau, P.-E. Mazeran, S. Bouvier, and A. Iost, "Effect of surface roughness in the determination of the mechanical properties of material using nanoindentation test," *Scanning*, vol. 36, no. 1, pp. 134–149, Jan. 2014, doi: https://doi.org/10.1002/sca.21111.
26. R. M. D. Zebaze *et al.*, "Intracortical remodelling and porosity in the distal radius and post-mortem femurs of women: a cross-sectional study," *The Lancet*, vol. 375, no. 9727, pp. 1729–1736, May 2010, doi: 10.1016/S0140-6736(10)60320-0.
27. A. A. F. Ogaili, M. N. Hamzah, and A. A. Jaber, "Free vibration analysis of a wind turbine blade made of composite materials," in *International Middle Eastern Simulation and Modelling Conference 2022, MESM 2022*, 2022, pp. 203–209. [Online]. Available: https://www.scopus.com/inward/record.uri?eid=2-s2.0-85145663562&partnerID=40&md5=861bd3792964daae94fe97ba01682a6d
28. T. M. Link, B. B. Koppers, T. Licht, J. Bauer, Y. Lu, and E. J. Rummeny, "In vitro and in vivo spiral CT to determine bone mineral density: Initial experience in patients at risk for osteoporosis," *Radiology*, vol. 231, no. 3, pp. 805–811, Jun. 2004, doi: 10.1148/radiol.2313030325.
29. A. Basillais *et al.*, "Three-dimensional characterization of cortical bone microstructure by microcomputed tomography: validation with ultrasonic and microscopic measurements," *Journal of Orthopaedic Science*, vol. 12, no. 2, pp. 141–148, 2007, doi: 10.1007/s00776-006-1104-z.
30. M. J. Turunen *et al.*, "Bone mineral crystal size and organization vary across mature rat bone cortex," *J. Struct. Biol.*, vol. 195, no. 3, pp. 337–344, 2016, doi: https://doi.org/10.1016/j.jsb.2016.07.005.
31. A. A. F. Ogaili, Q. S. Mahdi, E. S. Al-Ameen, A. A. Jaber, and E. K. Njim, "Finite-element investigations on the influence of material selection and geometrical parameters on dental implant performance," vol. 11, no. 1, 2024, doi: doi:10.1515/cls-2024-0015.
32. A. K. Sinha and G. Pamnani, "Applications of XFEM in Fracture Analysis: A Review," *Iran J Sci Technol Trans Civ Eng*, 2025, https://doi.org/10.1007/s40996-025-01955-7.
E. M. Feerick, X. (Cheryl) Liu, and P. McGarry, "Anisotropic mode-dependent damage of cortical bone using the extended finite element method (XFEM)," *J. Mech. Behav. Biomed. Mater.*, vol. 20, pp. 77–89, 2013, doi: https://doi.org/10.1016/j.jmbbm.2012.12.004.
33. J. Schwiedrzik *et al.*, "In situ micropillar compression reveals superior strength and ductility but an absence of damage in lamellar bone," *Nat. Mater.*, vol. 13, no. 7, pp. 740–747, 2014, doi: 10.1038/nmat3959.
34. Abdellatif HARIF and Moulay Abdellah KASSIMI, "Predictive Modeling of Student Performance Using RFECV-RF for Feature Selection and Machine Learning Techniques," *International Journal of Advanced Computer Science and Applications (IJACSA) 15.7*, 2024, http://dx.doi.org/10.14569/IJACSA.2024.0150723.
35. T. L. Anderson and T. L. Anderson, *Fracture Mechanics: Fundamentals and Applications*. CRC press, 2005.
36. A. Valizadeh *et al.*, "Failure criterion for assessing mixed mode fracture in cracked orthotropic materials," *Int J Solids Struct*, vol. 325, p. 113701, 2025, https://doi.org/10.1016/j.ijsolstr.2025.113701.
37. E. E. Gdoutos, *Fracture mechanics: an introduction*, vol. 263. Springer Nature, 2020.
38. M. Levy and Z. Yosibash, "Heterogeneous fracture toughness of human cortical bone tissue," *Int J Fract*, vol 249, no. 17, 2025, https://doi.org/10.1007/s10704-024-00836-w.
39. F. Ali, H. Yasmin, M. Mohialden, N. M. Hussien, F. A. Hashim, and Y. M. Mohialden, "Hybrid feature selection and ensemble classification for climate change indicators: A machine learning approach," *Terra Joule Journal*, vol. 1, no. 2, p. 8, Sep. 2025, doi: 10.64071/3080-5724.1021.
40. M. Böhme *et al.*, "Automatic segmentation of cortical bone microstructure: Application and analysis of three proximal femur sites," *Bone*, vol. 193, p. 117404, 2025, https://doi.org/10.1016/j.bone.2025.117404.
41. P. Zioupos and J. D. Currey, "Changes in the stiffness, strength, and toughness of human cortical bone with age," *Bone*, vol. 22, no. 1, pp. 57–66, Jan. 1998, doi: 10.1016/S8756-3282(97)00228-7.
42. A. G. Reisinger, D. H. Pahr, and P. K. Zysset, "Principal stiffness orientation and degree of anisotropy of human osteons based on nanoindentation in three distinct planes," *J. Mech. Behav. Biomed. Mater.*, vol. 4, no. 8, pp. 2113–2127, 2011, doi: https://doi.org/10.1016/j.jmbbm.2011.07.010.
43. G. Pellegrino, M. Roman, and J. C. Fritton, "Effects of the basic multicellular unit and lamellar thickness on osteonal fatigue life," *J. Biomech.*, vol. 60, pp. 116–123, 2017, doi: https://doi.org/10.1016/j.jbiomech.2017.06.006.
44. B. Coburn and R. R. Salary, "Mechanical characterization of porous bone-like scaffolds with complex microstructures for bone regeneration," *Bioengineering*, vol. 12, no. 4, 2025, doi: 10.3390/bioengineering12040416.
45. L. Breiman, "Random forests," *Mach. Learn.*, vol. 45, no. 1, pp. 5–32, 2001, doi: 10.1023/A:1010933404324.
46. B. G. Mejbel, S. A. Sarow, M. T. Al-Sharify, L. A. Al-Haddad, A. A. F. Ogaili, and Z. T. Al-Sharify, "A data fusion analysis and random forest learning for enhanced control and failure diagnosis in rotating machinery," *Journal of Failure Analysis and Prevention*, 2024, doi: 10.1007/s11668-024-02075-6.
47. S. T. Bunyan *et al.*, "Intelligent thermal condition monitoring for predictive maintenance of gas turbines using machine learning," *Machines*, vol. 13, no. 5, 2025, doi: 10.3390/machines13050401.

48. A. Koeppe, F. Bamer, M. Selzer, B. Nestler, and B. Markert, “Explainable artificial intelligence for mechanics: Physics-explaining neural networks for constitutive models,” *Front. Mater.*, vol. Volume 8-2021, 2022, [Online]. Available: https://www.frontiersin.org/journals/materials/articles/10.3389/fmats.2021.824958
49. E. Guzmán-Muñoz *et al.*, “Supervised machine learning-based prediction of in-hospital mortality following hip fracture in older adults,” *diagnostics*, vol. 16, no. 4, 2026, doi: 10.3390/diagnostics16040612.
50. A. O. Panhwar, S. Memon, L. Das Dhomeja, N. Memon, and A. A. Chandio, “Deep learning-based image segmentation techniques for bone fractures using X-ray images: A systematic review: Deep learning-based image segmentation techniques for bone fractures using X-ray images: A systematic review,” *VFAST Transactions on Software Engineering*, vol. 12, no. 4, pp. 99–116, Dec. 2024, doi: 10.21015/vtse.v12i4.1971.
51. H. Bayesteh and S. Mohammadi, “XFEM fracture analysis of orthotropic functionally graded materials,” *Compos. B Eng.*, vol. 44, no. 1, pp. 8–25, Jan. 2013, doi: 10.1016/j.compositesb.2012.07.055.